accepted in Physics of Fluids, 3 August 2021

Experimental investigation on backflow of power-law fluids in planar fractures

A. Lenci,[1] L. Chiapponi,[2] S. Longo,[2, a)] and V. Di Federico[1, b)]
[1)] *Dipartimento di Ingegneria Civile, Ambientale e dei Materiali (DICAM), Università di Bologna, viale Risorgimento 2, Bologna, Italy.*
[2)] *Dipartimento di Ingegneria Civile e Architettura (DIA), Università di Parma, Parma, Italy*

(Dated: 3 August 2021)

In hydrofracturing, we model backflow of a non-Newtonian fluid in a single flat-walled fracture of planar geometry and support our conceptualization with laboratory experiments. We consider a power-law fluid, a spatially homogeneous fracture aperture, and its variation in time depending on the internal fluid pressure and the elastic relaxation of the walls. The relationship between the latter quantities may be linear, akin to a Winkler soil, or nonlinear, due to the progressive softening or stiffening of the boundary associated with the properties of the surrounding rock. The result is an integro-differential problem that generally admits a closed-form solution, albeit implicit for some quantities. In particular, a comparison is conducted between the drainage time in the present configuration and point drainage in radial geometry. The approach is generalized by introducing leak-off, i.e. a loss of fluid at the fracture boundaries that accelerates the fracture closure, when compared to the no leak-off case. To validate the theoretical results, 14 experiments are conducted with an ad-hoc replica of a rectangular fracture of aspect ratio 2.5-2.7, with a maximum height of ≈ 2 mm; the elastic reaction of the walls is due to o-rings, also sealing the fracture without adding friction disturbances. Fluids with different rheology, both Newtonian and shear-thinning, are associated with different boundary conditions of external pressure and overload. The match between theory and experiments is fairly good, with discrepancies of a few percent essentially due to the approximations of the theoretical model, and, for shear-thinning fluids, to the simplified constitutive equation.

I. INTRODUCTION

Backflow is a term used in the hydrofracturing jargon to represent the third phase of the process following the injection of i) the fracturing fluid and ii) of the proppant (see Sahai and Moghanloo[1] and bibliography therein for a recent review). The first phase opens up new fractures, cracks and preferential pathways in the rock mass with a process that initiates at the main well, or borehole, typically located at 1-2 km below ground and having a sub-horizontal orientation; the second phase props them open. At the beginning of the third phase, the injection ceases and the downstream pressure gradient attenuates and then reverses its direction; this causes part of the fracturing fluid to flow back sequentially from matrix to fractures, fractures to well bore, and finally from well bore to surface, where the fluid is treated and re-used; the phenomenon is commonly described as backflow. The unrecovered portion of hydrofracturing fluid lost as formation leak off represents an economic loss[2] as well as a source of environmental pollution: the latter key aspect is clearly summarized by Birdsell *et al.*[3]. During the fourth and final phase, the product of the reservoir under exploitation, typically oil, gas or heat for the deepest reservoirs[4], follows the backflow and invades the fracture network, eventually reaching the borehole and initiating the productive stage. Any residual fracturing fluid retained in the fracture network or in the formation pore space, as well as the presence of proppant within the fractures[5], brings about a reduction of the fracture conductivity, impairing productivity and favouring the stagnation of the fracturing fluid in the subsurface.

While a variety of models examine with varying realism and at various scales (for a review see Britt[6] and Detournay[7]) the first phase of the hydrofracturing process, the details of backflow were investigated to a lesser degree of attention. In essence, it is seen that typically the reverse flow causes a pressure reduction within the formation and the fracture network upstream of the borehole; this in turn produces the relaxation of the walls, further squeezing the fracture and driving the fluid out. This phenomenon can be captured by numerical models based on a detailed knowledge of the fracture network[8], possibly based on AI techniques (see Agwu *et al.*[9] for a review concerning similar fluids); or represented by models of reduced complexity, characterized by a relatively low number of parameters. This second category includes the model of Lai *et al.*[10] for radial crack propagation and resulting backflow, the seminal work of Dana *et al.*[11], describing the same phenomena in a fracture network built as a succession of plane branches of increasing order, where at each order i two fractures branch out from an order $i-1$ fracture, reminiscent of river networks[12], and blood vessels or other biological systems (see Abugattas *et al.*[13] and references therein). The model was later extended to include variability in the branching parameters at each order[14]. The effect of a bifurcation on single and two-phase flow in a fracture surrounded by a porous medium was investigated by Zhu *et al.*[15]. Quite surprisingly, relatively few scientific works include non-Newtonian effects, despite the fact that hydrofracturing fluids are rheologically complex by definition. In the first place, they are often engineered so that their viscosity varies over time, typically due to

[a)] http://www2.unipr.it/~slongo/English_version/Sandro Longo.htm.
[b)] Author to whom correspondence should be addressed: vittorio.difederico@unibo.it

carefully planned chemical reactions within the fluid and/or with the rock matrix[16]. This peculiar characteristic permits the optimization of hydrofracturing operations: during the injection phase, a high viscosity allows formation of a clearly defined network of cracks without too much loss of fluid in the surrounding matrix, while in the backflow phase a low viscosity is desirable to minimize pressure losses and maximize the fluid recovery. In principle, this does not necessarily imply a non-Newtonian behaviour, characterized by a viscosity dependent on the velocity vector, or equivalently, by a nonlinear relationship between the stress and the velocity deformation tensors. In practice, however, the rheology of fracturing fluids is mostly non-Newtonian, as explained in detail e.g. by Osiptov[17]: this is linked to the desirable characteristics of non-Newtonian fluids, whose richness of descriptive parameters allows achieving several engineering objectives at the same time[18].

The adoption of complex constitutive models more apt to represent the rheology of the fracturing fluid has become common[19] in modelling all phases of the hydrofracturing process. At the scale of an entire formation, or of a domain including several formations, the approach is mostly numerical and includes a detailed description of the newly formed fracture network[20], interacting with the surrounding rock matrix and the fractures possibly already existing in the formation[21]. The rheological model adopted is usually power-law, the least detailed model incorporating a nonlinear relationship between stress and strain[22]. More detailed formulations, often based on an analytical or semi-analytical approach, focus on a single phase of the hydrofracturing process. In the injection phase, the formation of a plane-strain fracture driven by a power-law fluid is described by Adachi and Detournay[23] and Garagash[24], and by Mikhailov *et al.*[25] with the inclusion of leakoff; anisotropy in the rock matrix was then incorporated in the solution by Dontsov[26], while Lakhtychkin *et al.*[27] modelled the fracture expansion under the action of two proppant-laden immiscible power-law fluids. An alternative, numerical approach for the propagation phase was adopted by Perkovska[28]. More realistic, and complex rheological models, such as truncated power-law and Carreau, were only recently applied to single fracture propagation[29–31]. Much less developed are models for non-Newtonian backflow. To our knowledge, the first was presented by Chiapponi *et al.*[32], who modelled radially converging backflow of a non-Newtonian power-law fluid towards a borehole in a single disk-shaped fracture, checking their theoretical findings against laboratory experiments with satisfactory results. Later, Ciriello *et al.*[33] developed a similar analysis for plane flow of a non-Newtonian fluid described by the Ellis three-parameter model[34,35]. Here, we consider the same plane geometry and develop novel closed-form expressions for a power-law fluid, widely applied in porous and fractured media flow[36] with satisfactory results when the rheological parameters in the measuring device are estimated at the same shear rate range of the real phenomenon. We then verify our theoretical result by means of two ad hoc built experimental devices, describing its structure and calibration, exploring different types of wall reaction, and finding a good agreement between experiments and theory.

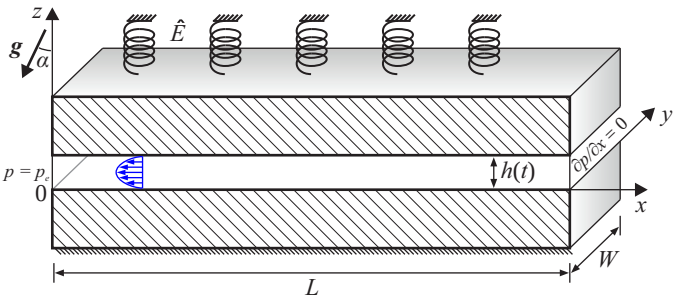

FIG. 1. Sketch of a smooth fracture with uniform aperture varying over time and elastic wall behaving as a linear/nonlinear ($\lambda = 1/\neq 1$) foundation of assigned coefficient of subgrade reaction $\hat{E}$ of dimensions $[ML^{-1-\lambda}T^{-2}]$, reverting to a Winkler coefficient $\tilde{E}$ of dimensions $[ML^{-2}T^{-2}]$ for $\lambda = 1$.

The manuscript is structured as follows. Section 2 includes the formulation of the problem and the derivation of i) the pressure field in the space/time and ii) the closure pattern of the fracture over time. Section 3 illustrates the experimental set-up, the measurement techniques for the rheological behaviour of the investigated fluids, interpreted with the Newtonian and power-law constitutive equations, and the experimental results with associated uncertainty. Section 4 illustrates a generalization of the problem, including the effects of leak-off from the fracture. Section 5 presents our conclusions and perspectives for future work. Appendices A-C provide additional details on the problem investigated.

II. POWER-LAW FLUID FLOW

A. Formulation

A fluid-filled, rigid rock fracture of length L, width W, time variable aperture $h(t)$ of starting value h_0, and elastic walls is initially ($t = 0$) subject to a no-flow condition at its end $x = L$ and to uniform initial pressure p_e imposed by the value at its outlet $x = 0$, connected with the main well or borehole (see Figure 1). The backflow towards the borehole causes a pressure reduction within the fracture that in turn produces the relaxation of the walls, further squeezing the fracture. For a given time, the pressure is $p(x,t)$, while the fracture volume and the outflowing discharge per unit width are $V_f = Lh$ and $q = -dV_f/dt = -L\ dh/dt$. Hereinafter, the pressure within the fracture is taken to include gravity effects (reduced or generalized pressure) caused by the inclination α of the fracture with respect to the horizontal plane. Note that this assumption can be adopted also for the radial geometry, adding generality to the results of Chiapponi *et al.*[32] without the need for neglecting gravity effects.

The fracture aspect ratios are $\varepsilon_1 = L/W \ll 1$ and $\varepsilon_2 = h/L \ll 1$, and the lubrication approximation holds. Hence, the flow is one-dimensional in the x direction; this allows concentrating the relaxation of the fracture entirely in one of the two walls, taken to be the upper one for pure convenience. We further assume that the plane fracture under consideration

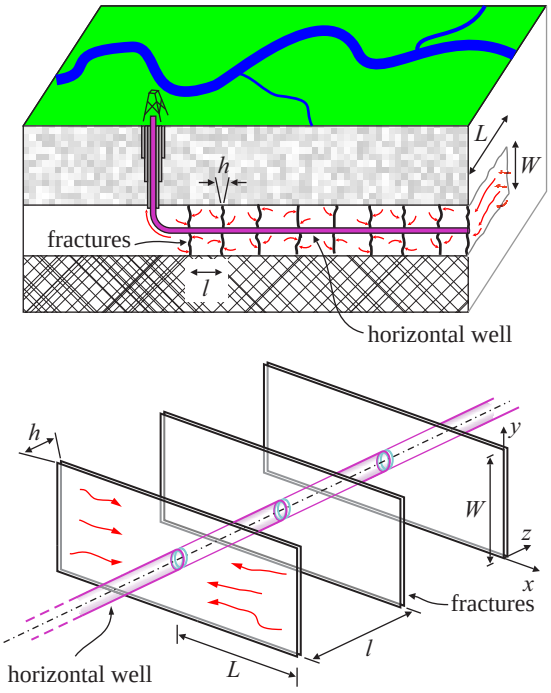

FIG. 2. Bi-wing planar and symmetric fractures of dimensions L, W and h and equal spacing l originating from a horizontal borehole; here $\alpha = 90^\circ$ as the fractures lie in the vertical plane.

belongs to a series of evenly distributed fractures of spacing l with respect to a horizontal borehole or main well, as it is most often the case in hydraulic fracturing (see Figure 2).

To represent in a general form the reaction of the wall we adopt the formulation of Ciriello *et al.*[33], allowing for generality the Young modulus E of the rock wall to be a function of the strain rate, according to the power-law relationship

$$E = E_0 \left(\frac{h}{l}\right)^{\lambda-1}, \tag{1}$$

where E_0 is a reference value of the Young modulus of dimensions $[ML^{-1}T^{-2}]$ and λ a non-negative constant governing the type of wall reaction: linear for $\lambda = 1$, sub-linear or supra-linear for $0 < \lambda < 1$ or $\lambda > 1$ respectively. It is worth noting that $\lambda \neq 1$ also represents possible experimental constraints. Under a Winkler conceptualization of subgrade springs illustrated in Figure 1, the rigid wall reacts to the upward fluid pressure with a downward pressure proportional to the aperture given by $r(t) = \tilde{E}h$ where $\tilde{E}$ is the coefficient of subgrade reaction of dimensions $[ML^{-2}T^{-2}]$. For a thin elastic layer, this coefficient is given by the ratio between the Young modulus of the layer's material E $[ML^{-1}T^{-2}]$ and its thickness l[37], i.e.

$$\tilde{E} = E/l, \tag{2}$$

where l in this context is identified with the fracture spacing[32]. The actual validity, albeit approximate, of eq. (2) is conditioned on $l/L < 1$, a requirement often respected in artificial fracture networks produced by fracking (see Ciriello *et al.*[33] and references therein).

The wall equilibrium, written per unit width, then requires

$$\int_0^L p(x,t)\,\mathrm{d}x = r(t)L = \tilde{E}Lh(t), \tag{3}$$

or equivalently using eqs. (1)-(2)

$$\int_0^L p(x,t)\,\mathrm{d}x = \hat{E}Lh^\lambda(t), \tag{4}$$

where $\hat{E} = E_0 l^{-\lambda}$ of dimensions $[ML^{-1-\lambda}T^{-2}]$ is a coefficient of subgrade reaction under the assumption of nonlinear wall reaction and evenly spaced fractures, and reverts to the physical meaning and dimensions of a Winkler subgrade coefficient if $\lambda = 1$. Note that eq. (4) stands by itself in the case of a single fracture when the spacing l is not defined and there is no need of eqs. (1), (2) and (3). The wall equilibrium is further generalized by adding a constant force per unit width, defined as overload f_0, on the right-hand side of (4), typically opposing the fracture aperture and associated for instance to a residual state of stress within the rock wall generated by its load history. Eq. (4) then becomes,

$$\int_0^L p(x,t)\,\mathrm{d}x = \hat{E}Lh^\lambda(t) + f_0, \tag{5}$$

completing the schematization of the fluid-wall interaction.

Turning now our attention to the flow, inertial effects are negligible, the regime is viscous, and the fluid has a power-law rheology, described in simple shear flow by the constitutive equation

$$\tau_{zx} = -\tilde{\mu}|\partial u/\partial z|^{n-1}\partial u/\partial z, \tag{6}$$

with τ_{zx} shear stress, u velocity, $\tilde{\mu}$ consistency index and n flow behaviour index; for $n = 1$ the fluid is Newtonian, for $n < 1$ shear-thinning, for $n > 1$ shear-thickening. Under the previous assumptions, the pressure distribution is hydrostatic and the velocity profile at any cross-section x is

$$u(x,z,t) = -\frac{n}{2^{(n+1)/n}(n+1)}\frac{1}{\tilde{\mu}^{1/n}}\left|\frac{\partial p}{\partial x}\right|^{1/n-1} \times \frac{\partial p}{\partial x}\left(h^{(1+n)/n} - |2z-h|^{(1+n)/n}\right). \tag{7}$$

Shear-thinning fluids ($n < 1$) are most common in practical applications and will be considered henceforth. The wall velocity w_w perpendicular to the wall itself is initially zero at the start of the relaxation phenomenon, i.e.

$$w_w(0) = 0, \tag{8}$$

and is given at the generic time t by

$$w_w(h) = \frac{\partial h}{\partial t} = \frac{\mathrm{d}h(t)}{\mathrm{d}t}, \tag{9}$$

the last equality holding as the wall is rigid. Further, w_w is related to the fluid velocity u in the x direction by the principle of continuity

$$\frac{\partial w_w}{\partial z} + \frac{\partial u}{\partial x} = 0. \tag{10}$$

Substituting eqs. (7) and (9) in eq. (10) and integrating perpendicular to the wall between $z=0$ and $z=h(t)$ with the boundary conditions (8)-(9) yields

$$\frac{\mathrm{d}h(t)}{\mathrm{d}t} = \frac{1}{2^{(1+n)/n}(2n+1)\tilde{\mu}^{1/n}} h(t)^{(2n+1)/n} \times \left|\frac{\partial p(x,t)}{\partial x}\right|^{1/n-1} \frac{\partial^2 p(x,t)}{\partial x^2}. \quad (11)$$

Referring now again to the geometry described by Figure 2, showing several bi-wing planar fractures (the schemes for single or multiple fractures do not differ except for the quantities depending on the spacing l), it is noted that consistently with the assumption $L \gg W$ the flow is uniform along most of the fracture half-length L and may be approximately described as planar except in the vicinity the well. Neglecting the convergence of flow lines therein allows simplifying the boundary condition at the fracture outflow, so that the initial and boundary conditions to eqs. (5) and (11) read

$$h(0,t) = h_0, \quad p(0,t) = p_e, \quad \frac{\partial p(x,t)}{\partial x}(L,t) = 0, \quad (12)$$

where i) h_0 is the initial fracture aperture; ii) p_e is the pressure at the fracture outflow, taken to be equal to borehole pressure along the entire fracture height W; iii) the condition at the fracture inflow, representing the upstream network of fractures created by the injection process, is identified as a zero pressure gradient, the least impacting condition on the pressure within the fracture.

B. Solution

The governing equations (5) and (11), and the initial and boundary conditions (12) can be written in dimensionless form respectively as

$$\frac{1}{H(T)^{(2n+1)/n}} \frac{\mathrm{d}H(T)}{\mathrm{d}T} = \left|\frac{\partial P(X,T)}{\partial X}\right|^{(1-n)/n} \frac{\partial^2 P(X,T)}{\partial X^2}, \quad (13)$$

$$\int_0^1 P(X,T)\mathrm{d}X = H^{\lambda}(T) - P_e + F_0, \quad (14)$$

$$H(X,0) = 1, \quad P(0,T) = 0, \quad \frac{\partial P(X,T)}{\partial X}(1,T) = 0, \quad (15)$$

by using the dimensionless quantities

$$X = x/L, H = h/h_0, T = t/t_c, P = (p-p_e)/p_c, \quad P_e = p_e/p_c, F_0 = f_0/(Lp_c), Q = (qt_c)/(Lh_0). \quad (16)$$

In eq. (16), the time and pressure scales t_c and p_c are defined as

$$t_c = \left(\frac{\tilde{\mu}}{\hat{E}}\right)^{1/n} \frac{(2L)^{(n+1)/n}(2n+1)}{h_0^{(n+\lambda+1)/n}}, \quad p_c = \hat{E}h_0^{\lambda}. \quad (17)$$

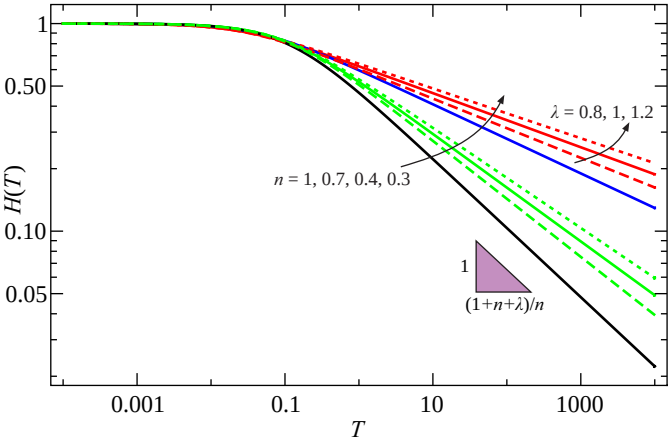

FIG. 3. Dimensionless fracture aperture versus dimensionless time for $P_e - F_0 = 0$, and $n = 1, 0.7, 0.4, 0.3$. The cases $\lambda = 0.8, 1, 1.2$ are represented by dashed, continuous and dotted lines for $n = 0.7$ and $n = 0.3$ to illustrate the dependence upon λ.

To solve the problem an auxiliary function is defined as

$$G(T) = \frac{1}{H(T)^{(2n+1)/n}} \frac{\mathrm{d}H(T)}{\mathrm{d}T}. \quad (18)$$

Together with the assumption of backflow, implying $\partial P/\partial x > 0$, eq. (18) allows integrating eq. (13) with the boundary conditions in eq. (15), obtaining the pressure field

$$P(X,T) = \frac{[-G(T)]^n}{n^n(n+1)} \left[1-(1-X)^{n+1}\right]. \quad (19)$$

Substituting eqs. (18) and (19) into eq. (14) gives

$$\frac{\mathrm{d}H}{\mathrm{d}T} + n(n+2)^{1/n} H^{(2n+1)/n} \left(H^{\lambda} - P_e + F_0\right)^{1/n} = 0, \quad (20)$$

subject to the initial condition in eq. (15).

For $P_e - F_0 = 0$ eq. (20) admits the following closed-form solution

$$H(T) = \left[1 + (1+n+\lambda)(n+2)^{1/n} T\right]^{-n/(1+n+\lambda)}, \quad (21)$$

and consequently the pressure is given by

$$P(X, H(T)) = \frac{n+2}{n+1} H^{\lambda}(T) \left[1-(1-X)^{n+1}\right]. \quad (22)$$

For $n = 1$ and $\lambda = 1$, equations (21) and (22) reduce to the expressions derived by Dana *et al.*[11] for a Newtonian fluid and $\lambda = 1$ (a linearly elastic wall). Appendix A reports their late-time ($T \gg 1$) approximations. The dimensionless fracture aperture is shown versus time in Figure 3, showing the late-time $T^{-n/(n+\lambda+1)}$ scaling; the smaller the flow behaviour index n, the larger the dimensionless aperture. For smaller λ

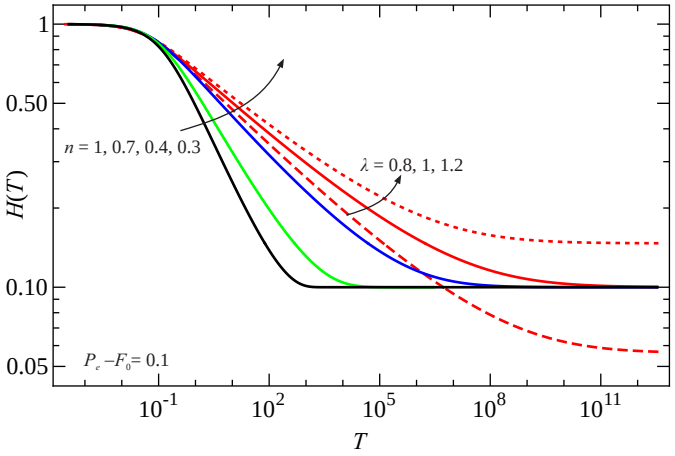

FIG. 4. Dimensionless fracture aperture versus dimensionless time for $P_e - F_0 = 0.1$ and $n = 1, 0.7, 0.4, 0.3$. The cases $\lambda = 0.8, 1, 1.2$ are represented by dashed, continuous and dotted lines for $n = 0.7$ and $n = 0.3$ to illustrate the dependence upon λ.

values, the fracture aperture decreases faster with time as the wall reacts less.

For $P_e - F_0 \geq 0$, the function $H(T)$ is obtained implicitly as

$$T = \frac{1}{(n+2)^{\frac{1}{n}}(1+n+\lambda)} \left[\frac{1}{\zeta^{(1+n+\lambda)/n}} \times {}_2F_1\left(\frac{1}{n}, \frac{1+n+\lambda}{n\lambda}; \frac{(1+\lambda)(n+1)}{n\lambda}; \frac{P_e - F_0}{\zeta^{\lambda}}\right)\right]\Bigg|_1^H, \quad (23)$$

where ζ is a dummy variable, ${}_2F_1(a,b;c;\zeta)$ is the hypergeometric function of parameters a, b, c and argument ζ and the linear transformation (9.132.2) in Gradshteyn and Ryzhik[38] has been used. Early- and late-time approximation of the general equation (23) are reported in Appendix B. For the special case $P_e - F_0 = 0$, eq. (23) becomes eq. (21); for $n = 1$ and $\lambda = 1$, it reduces to equation (2.18) in Dana *et al.*[11] via the identity in Appendix C. When a linear wall reaction ($\lambda = 1$) is coupled with a shear-thinning fluid ($n < 1$), eqs. (21) and (23) reduce to

$$H(T) = \left[1 + (n+2)^{(n+1)/n} T\right]^{-n/(n+2)}, \quad (24)$$

$$T = \frac{1}{(n+2)^{\frac{n+1}{n}}} \times \left[\frac{1}{\zeta^{(n+2)/n}} {}_2F_1\left(\frac{1}{n}, \frac{n+2}{n}; \frac{2(n+1)}{n}; \frac{P_e - F_0}{\zeta}\right)\right]\Bigg|_1^H. \quad (25)$$

The behaviour of the aperture-time function is depicted in Figure 4 for different values of n and λ and the case $P_e - F_0 = 0.1$. The aperture tends for large times to $(P_e - F_0)^{1/\lambda}$, and reaches this asymptote later for as the fluid becomes more shear-thinning; the asymptote value is larger when the wall is more rigid (larger λ).

The pressure field for the general case $P_e - F_0 > 0$ is

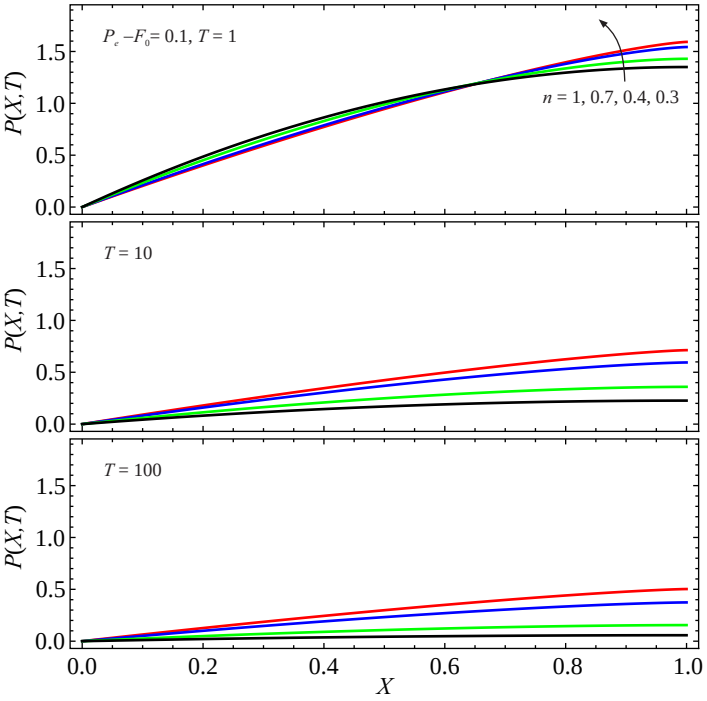

FIG. 5. Pressure field for $P_e - F_0 = 0.1$, $n = 1, 0.7, 0.4, 0.3$ and $\lambda = 1$.

$$P(X, H(T)) = \frac{n+2}{n+1} H^{\lambda}(T) \left[1 - \frac{P_e - F_0}{H^{\lambda}(T)}\right] \left[1 - (1-X)^{n+1}\right]. \quad (26)$$

Upon plotting the spatial trend of dimensionless pressure within the fracture at different times (Figure 5), it is observed that the pressure increases along the fracture and decreases over time; this decrease markedly depends on the value of n and is slower for shear-thinning fluids, more so at late times, while at early times the pressure difference among different fluids is modest.

C. Drainage analysis

A comparison between the efficiency of the linear and point drainage mechanisms[39], corresponding to the plane or radial geometry, may be readily obtained by confronting the corresponding solutions for zero outlet pressure and overload, the present eq. (21) and eq. (17) of Chiapponi *et al.*[32]. These two have the general format

$$H(T) = \frac{1}{[1 + \delta(n,\lambda) T]^{n/(1+n+\lambda)}}, \quad (27)$$

where the dependence on the drainage mechanism can be encapsulated in a decay coefficient $\delta(n,\lambda)$ for the fracture aperture, with $1/\delta$ akin to a dimensionless timescale of decay. In dimensionless terms, a larger decay coefficient implies a smaller aperture and residual pressure at any given time and location, hence a more efficient drainage mechanism. Figure 6 depicts the behaviour of $\delta(n,\lambda)$, showing that the decay

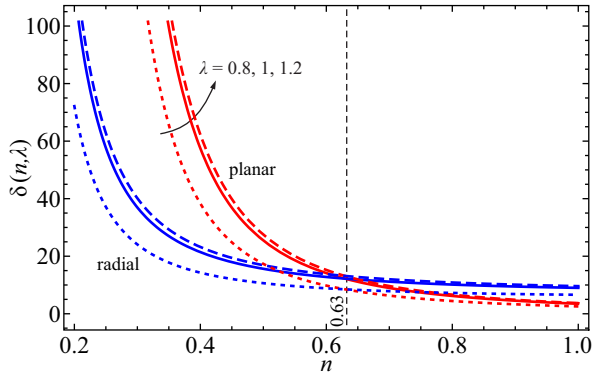

FIG. 6. Decay ratio for linear and point drainage within a planar fracture and a circular one. The curves refer to softening (dotted), linear (continuous) and stiffening (dashed) fracture wall.

rate: (i) decreases for increasing n, as the fluid behaviour approaches the Newtonian one, (ii) increases for increasing λ, as the fracture wall reacts more to any given pressure within the fracture, (iii) is more sensitive to the values of n and λ for small values of these two parameters, and (iv) is smaller for point than for linear drainage for shear-thinning fluids with $n < n_0 \lessapprox 0.63$. These results indicate that, above this threshold, the point drainage is less effective than the linear drainage. This is readily explained, as the average shear stress is homogeneous for the planar geometry with linear drainage, while it increases towards the origin for the radial geometry plate with point drainage. As the draining fluid becomes more shear-thinning, this effect is less pronounced than for Newtonian fluids, and eventually disappears for very shear-thinning fluids. It must be stressed that these conclusions refer exclusively to dimensionless results.

The outflowing discharge can be derived in dimensionless form and in analogy to Chiapponi *et al.*[32] as

$$Q = n(n+2)^{\frac{1}{n}} H^{\frac{2n+1}{n}} \left(H^{\lambda} - P_e + F_0\right)^{\frac{1}{n}}. \tag{28}$$

Analogously, the drainage time T_Y required to drain Y% of the total fracture volume ($0-100$% in dimensionless form) is equal to

$$T_Y = \frac{1}{(1+n+\lambda)(n+2)^{1/n}} \left[\left(\frac{100}{100-Y} \right)^{(1+n+\lambda)/n} - 1 \right], \tag{29}$$

for $P_e - F_0 = 0$, while for $P_e - F_0 \geq 0$ it is given by

$$T_Y = \frac{1}{(1+n+\lambda)(n+2)^{1/n}} \left[\frac{1}{\zeta^{(1+n+\lambda)/n}} \times {}_2F_1\left(\frac{1}{n}, \frac{1+n+\lambda}{n\lambda}; \frac{(1+\lambda)(n+1)}{n\lambda}; \frac{P_e - F_0}{\zeta^{\lambda}} \right) \right]_1^b, \tag{30}$$

with

$$b = (P_e - F_0)^{1/\lambda} + \frac{100-Y}{100} \left[1 - (P_e - F_0)^{1/\lambda} \right]. \tag{31}$$

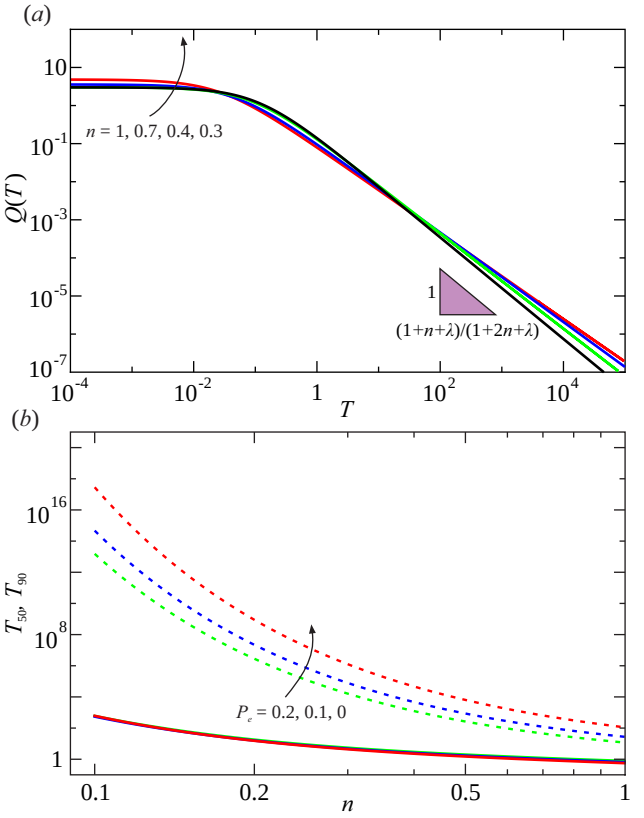

FIG. 7. *a*) Discharge out of the fracture versus time for $P_e = 0$, $F_0 = 0$, $n = 1, 0.7, 0.4, 0.3$, and $\lambda = 1$. *b*) Time T_{50} (continuous lines) and T_{90} (dashed lines) required to drain 50% and 90%of the total volume versus n, for $\lambda = 1$, $F_0 = 0$, and $P_e = 0, 0.1, 0.2$.

Figure 7*a* shows the dimensionless discharge out of the fracture for different values of n, zero outlet pressure P_e and overload F_0. The curves almost collapse, and according to eq. (28) exhibit an asymptotic scaling with time of exponent $-(2n+\lambda+1)/(n+\lambda+1)$; special values are $-2(n+1)/(n+2)$ for $\lambda = 1$, $-(3+\lambda)/(2+\lambda)$ for $n = 1$, and $-4/3$ for $n = 1$ and $\lambda = 1$. Figure 7*b* depicts T_{50} and T_{90}, the times required to drain 50% and 90% of the total fracture volume, for different values of n and P_e with $F_0 = 0$. Results are extremely sensitive to the values of P_e and n; the time needed to achieve a certain recovery decreases as the shear-thinning fluid approaches Newtonian behaviour and drops by orders of magnitude as P_e increases. This may seem counterintuitive (the fracture drains against a non-zero outer pressure) but it happens as for $P_e > 0$ the fracture does not shut down completely, as opposed to the case $P_e = 0$. Note that in log-linear scale, the curves are practically indistinguishable for a 50% recovery, differ conspicuously for a 90% recovery, and even more so for a 99% recovery (not shown). For a softening model of the Winckler soil ($\lambda < 1$) there is a reduction of the drainage time with respect to the values computed for $\lambda = 1$, and the differences are greater the more the fluid is shear-thinning; the opposite is true for a stiffening model (not shown).

III. EXPERIMENTS

The theory was validated via a set of experiments run in the Hydraulics Laboratory of Parma University. The experimental setup is described in section 3.1, uncertainty quantification in 3.2, and the actual experimental results in 3.3.

A. Experimental setup

In order to verify the theoretical model and to highlight the possible limitations of the scheme, two experimental devices were built (hereinafter small and large apparata), both consisting of a rigid rectangular flat slat of aluminium alloy, which moves vertically in a sealed cylinder of the same material. The parts were manufactured via a numerically controlled machine (CNC) to guarantee the flatness of the surfaces and therefore the uniformity of the thickness of the rectangular gap.

The seal is created using a neoprene o-ring with a diameter of 6-8 mm, with seats that allow the elastic deformation of the o-ring in a range generally less than 2 mm. The elastic reaction of the fracture wall, a Winkler soil for $\lambda = 1$, is represented by the elastic reaction of the o-ring. The elastic reaction function is taken to be a power-law according to eq. (1), and is experimentally evaluated by injecting pressurized air, with pressure measured by a Druck calibrator DPI601 20 kPa full-scale, and by measuring the vertical position of the piston with 3 dial gauges with a resolution of 1/100 mm: for different values of the air pressure, different vertical positions of the piston were measured. The general interpolating function is $p = p_t + \hat{E}h^{\lambda}$, where p_t is a threshold pressure due to pre- compression of the o-rings. The effect of this threshold pressure is equivalent to an overweight f_0.

The small apparatus shown in figure 8 has an internal length of about $2L = 45$ cm and a width of about $B = 9$ cm. In order to ensure uniformity of the gap during testing, the outlet is in the middle of the cylinder, with the two draining trunks of about $L = 20$ cm length discharging symmetrically. Two neoprene o-rings are installed, one between the upper surface of the piston and the closing frame of the cylinder, the other between the lower surface of the piston and the cylinder (bottom neoprene o-ring), with elastic reactions of the o-rings in opposition. The weight of the piston is 20.20 N. A pressure tap at the bottom of the cylinder allows measurement of the initial pressure.

The large experimental apparatus, shown in figure 9, is missing the bottom neoprene o-ring, has an internal length of about $2L = 80$ cm and a width of about $B = 15$ cm. For this device, too, the outlet is in the centreline. In this apparatus, the o-ring is installed between the top surface of the piston and a closing frame of the cylinder (in the same configuration adopted for the first experimental device), with a free gap between the side walls of the piston and the cylinder of about 7/10 mm. The weight of the piston is 78.35 N. This large device has been realized both to check the existence of scale effects and to check the effects of the gap between the lateral surfaces of the piston and the cylinder; this gap could to some extent distort the main flow and could facilitate fluid drainage.

Prior to testing, the elastic reaction of the o-ring was calibrated, with a typical result shown in figure 10ab; the single o-ring in the large experimental apparatus shows a stiffening response, while the double o-ring in the small experimental apparatus exhibits an almost linear response.

To start an experiment, the inlet pipe was connected to a tank filled with the fluid and positioned at a variable height with respect to the bottom of the cylinder. The purge valves were initially opened to eliminate air bubbles in the fracture and in the hydraulic circuit. Then the valves were closed, and the piston slowly began to move upwards. After reaching the desired position of the piston, the inlet pipe was closed and the outlet pipe was opened rapidly to simulate backflow, with the piston moving downwards. The position in time of the piston was recorded with a video camera at 25 frames per second. The video frames were post-processed to extract the reading of the three dial gauges. For experiments where the external pressure was non-zero, the tank was quickly lowered.

The Newtonian fluids adopted in the experiments were obtained by mixing glycerol and water in different proportions to obtain different viscosities; the shear-thinning non-Newtonian fluids were obtained by adding Xanthan Gum to the above mixture. The rheological parameters were obtained via a parallel-plate rheometer by Anton Paar (dynamic shear rheometer Physica MCR 101), kept at the same temperature of the experiments. Fluid density was measured with a pycnometer.

B. Uncertainty quantification

The uncertainties of the experiments derive from the measurement procedures and from the parameters' estimation. The dials indicators have an absolute uncertainty assumed equal to the resolution of 1/100 mm; the absolute uncertainty in time measuring equals half the time step between two subsequent frames, 1/50 s. On the basis of the characteristics of the rheometer and of rheometric data dispersion, we assume a relative uncertainty in fluid behaviour index $\Delta n/n \leq 4\%$ and in consistency index $\Delta\tilde{\mu}/\tilde{\mu} \leq 6\%$. These uncertainties have been minimized by interpolating experimental rheometric data within the same range of shear rate of the experiments, see Longo *et al.*[36], yet are larger than the discrepancies typically associated to the adoption of a plate-plate geometry in lieu of a cone-plate geometry. The range of shear rate is computed considering that the maximum value at the wall is

$$\dot{\gamma}_w = \left(\frac{h}{2\tilde{\mu}}\right)^{1/n} \left(\frac{\mathrm{d}p}{\mathrm{d}x}\right)^{1/n}. \tag{32}$$

The gap-averaged value is $< \dot{\gamma} >= \dot{\gamma}_w[n/(n+1)]$, decays in time and decreases with the distance from the outlet section. Figure 11 shows the typical rheometric data for the shear-thinning fluid adopted in the present experiments, with two interpolating functions for two different ranges of the shear rate, and figure 12 shows the gap-average shear rate during Exp. 11.

The uncertainty in mass density measurement equals $1\,\mathrm{g\,cm^{-3}}$, with $\Delta\rho/\rho \leq 0.1\%$. The elastic response of the neo-

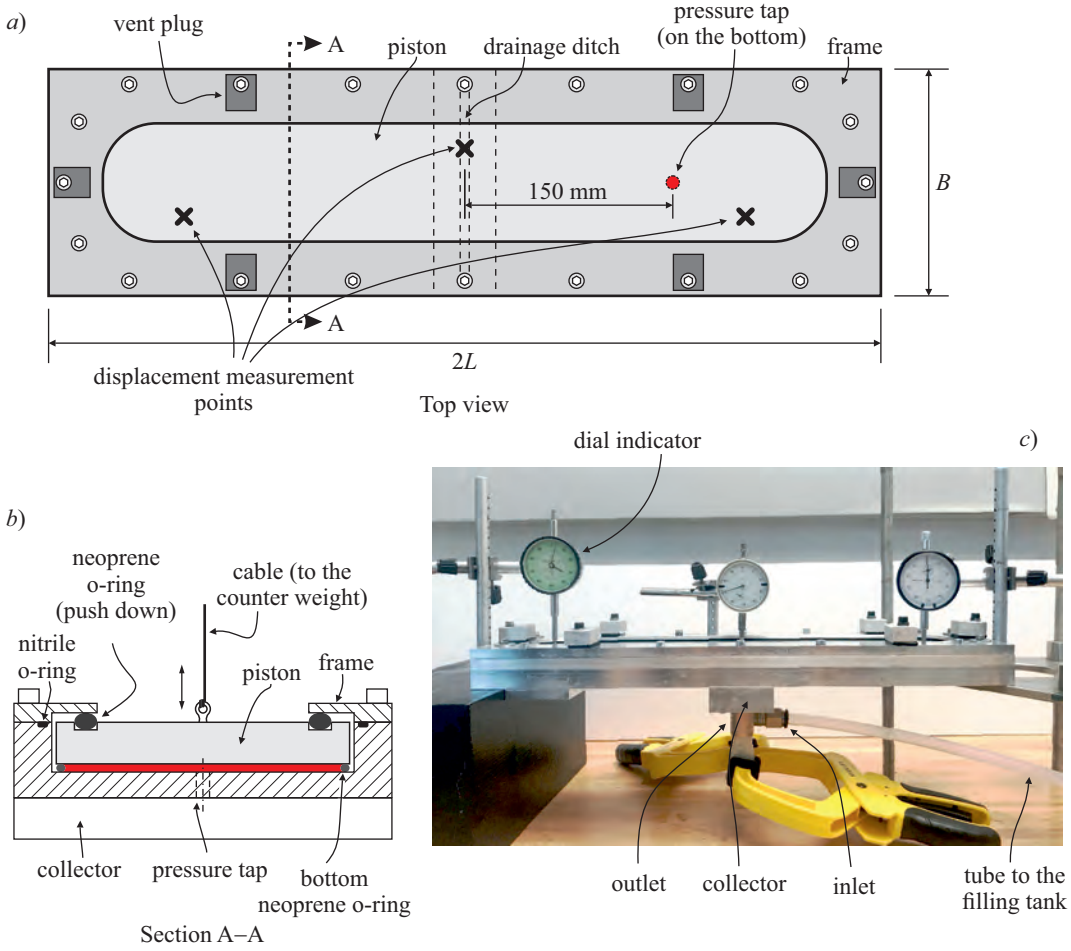

FIG. 8. Small experimental apparatus. *a*) Top view, *b*) cross view, and *c*) a photo of the apparatus during tests. The bottom neoprene o-ring is missing in the large experimental apparatus.

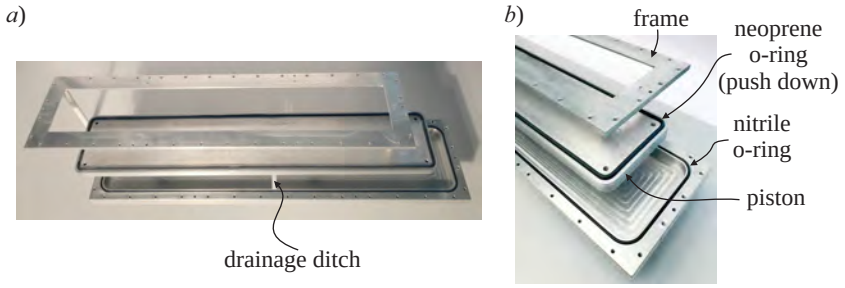

FIG. 9. Large experimental apparatus. *a*) General view, *b*) details of the frame, the piston and the cylinder.

prene o-ring is affected by partial hysteresis, which represents the most relevant source of uncertainty, with $\Delta\hat{E}/\hat{E} \leq 5.8\%$ and $\Delta\lambda/\lambda \leq 5.5\%$. Other sources of uncertainty are related to the accuracy of CNC machines and are difficult to quantify.

C. Comparison with model prediction

Fourteen tests were conducted, ten with a Newtonian and four with a shear-thinning fluid, with an initial fracture aperture ranging from 1.47 to 0.73 mm; four test had a non-zero external pressure. Table I lists the main parameters of the tests. The rheological parameters were obtained by interpolating the rheometrical data in the shear rate range of the experiments. With a similar approach, the elastic parameters $\hat{E}$ and λ were obtained by interpolating a power-function in the range of fracture aperture during the tests. We note that the reaction of the wall was always supra-linear, with λ in the range $1.10 \div 1.65$, for the ten tests with Newtonian fluids, and always sublinear, with λ in the range $0.60 \div 0.80$, for the four

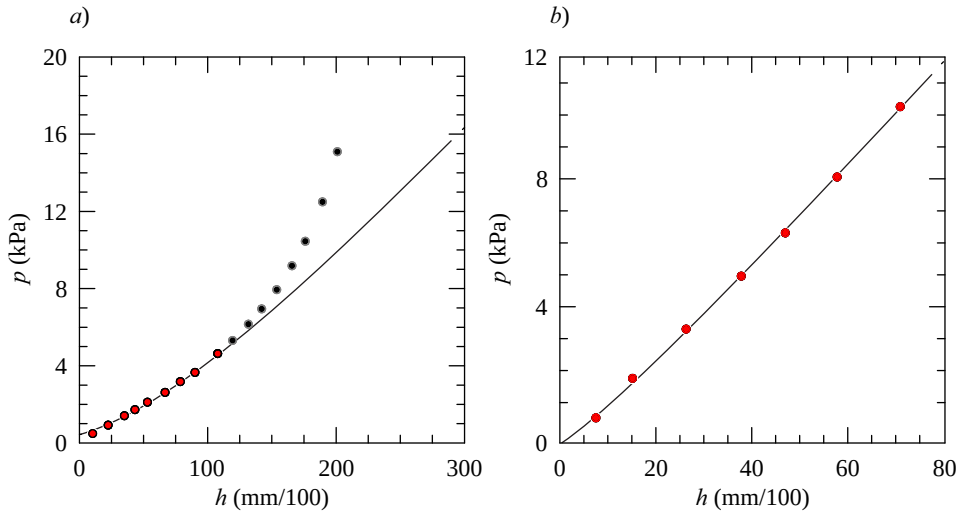

FIG. 10. Typical experimental elastic response of the system. *a*) Single neoprene o-ring (large experimental apparatus), and *b*) double o-ring in opposition (small experimental apparatus).

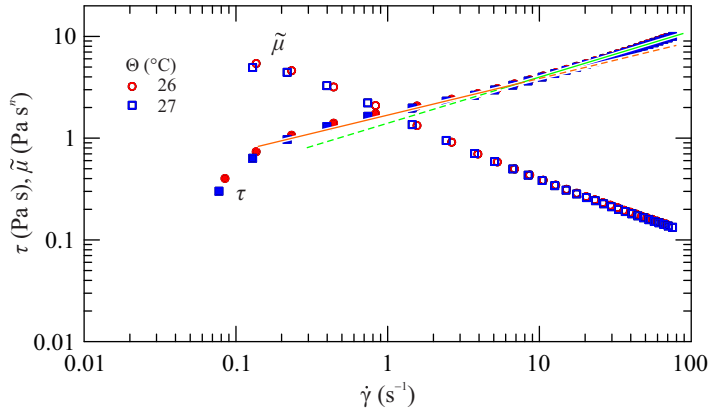

FIG. 11. Typical rheometric data for the shear-thinning fluid adopted in the experiments, measured at temperatures of 26°C and 27°C. The two interpolating lines indicate that the rheological parameters depend on the range of the shear rate.

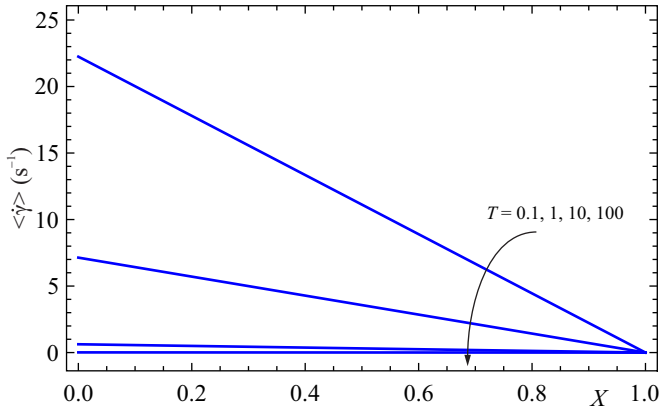

FIG. 12. Theoretical gap-average shear rate during backflow for Exp. 11, shear-thinning fluid.

tests with shear-thinning fluids. On the contrary, performing experiments in radial flow, the wall reaction was always linear[32]. This behaviour is dictated by the different geometry of the o-ring seat, with respect to the piston in radial geometry, while in the case of the small apparatus the presence of two o-rings in opposition reduces the value of λ. Exception is made for Exp. 8 for which also in the small apparatus only the upper o-ring was installed. An overload was always present, except for Exp. 6, since for this experiment the piston weight was balanced. Many different values of the Winkler subgrade coefficient $\hat{E}$ were employed, spanning more than three orders of magnitude. The large apparatus was always used with Newtonian fluids except for one case, while the small one was coupled with shear-thinning fluids in all cases. Using two apparata allowed us to verify the lack of scale effects, and to test two different sealing techniques, associated with different elastic responses.

The repeatability of the experiments turned out to be fairly good, as shown by the near overlap of the time series of the fracture aperture for Exp. 1 and 2 conducted under the same conditions except for h_0.

Figure 13 compares theoretical predictions and experimental results for the relationship between aperture and time; the two latter quantities are normalized. The experimental apertures match well their theoretical counterparts, capturing the decrease of the aperture versus time towards the respective asymptote; for some experiments there is a slight overestimation, for other experiments the opposite is true with no clear tendency. The same comparison is proposed in Figure 14 for shear-thinning fluids; again, the match between theory and experiments is fairly good, with no appreciable differences in accuracy between different experiments. Similarly, no clear trend towards under- or over-estimation is evident, with perhaps a tendency of the residual aperture to exceed the theoretical prediction.

Expt.	n	$\tilde{\mu}$ (Pa s^n)	Θ (°C)	ρ (g cm^{-3})	h_0 (mm)	p_e (Pa)	λ	$\hat{E}$ (MPa m$^{-\lambda}$)	p_t (Pa)	f_0 (N)	Apparatus
1	1	0.24	23.0	1.240	0.97	0	1.36	45.5	1200	78.35	L
2	1	0.24	23.0	1.240	0.73	0	1.36	45.5	1200	78.35	L
3	1	0.50	23.0	1.250	1.21	0	1.43	63.7	950	78.35	L
4	1	1.36	20.0	1.257	1.10	0	1.31	32.5	800	78.35	L
5	1	1.11	19.0	1.257	1.11	0	1.45	88.2	250	78.35	L
6	1	1.06	19.5	1.256	1.46	0	1.60	244.9	450	0.00	L
7	1	0.59	22.6	1.256	1.06	0	1.65	477.5	900	20.20	L
8	1	0.38	23.5	1.256	0.75	0	1.10	29.6	1000	20.20	S
9	1	0.51	22.0	1.250	0.98	2600	1.30	25.3	0	78.35	L
10	1	1.36	20.0	1.257	0.93	1200	1.15	10.9	0	78.35	L
11	0.42	1.52	26.3	1.175	0.98	0	0.69	1.3	0	20.20	S
12	0.46	1.56	27.0	1.175	1.26	11400	0.80	2.6	0	20.20	S
13	0.46	1.52	27.0	1.175	0.97	6700	0.80	2.6	0	20.20	S
14	0.6	1.90	27.0	1046	0.80	0	0.6	0.4	0	20.20	S

TABLE I. Parameters adopted for the tests in planar geometry. n and $\tilde{\mu}$ are the fluid behaviour and consistency indexes, Θ is the temperature during the test, ρ is the fluid density, h_0 is the initial fracture height, p_e is the external pressure during backflow, λ, $\hat{E}$ and p_t are the exponent characterizing the nonlinearity of the elastic response, the Winkler subgrade coefficient and the threshold pressure, with $p = p_t + \hat{E}h^{\lambda}$, where the threshold pressure is the minimum value of pressure required to lift the piston and is due to pre- compression of the o-rings; f_0 is the external load, positive if it favours the fracture closure. In the last column, the symbol "L" and "S" indicates that the large/small experimental apparatus was used.

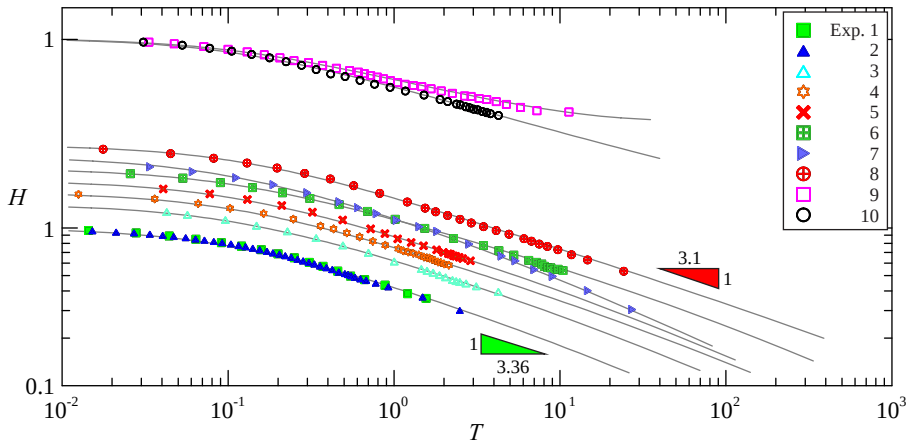

FIG. 13. Experimental results for the Newtonian fluid, with parameters listed in table I. Symbols represent the experimental data, curves are the theory. Expts. 1-8 are with zero exit pressure, Expts. 9-10 are with non-zero exit pressure. Data and theoretical curves are translated along the vertical for a better visualization, except for Expts.1 and 2, conducted under the same conditions to check the repeatability of the results.

IV. THE EFFECTS OF LEAK-OFF

A further refinement to the conceptual scheme is considering the additional effect of leak-off, with the fluid infiltrating the matrix surrounding the fractures, see Longo and Di Federico[40]. This loss of fluid potentially occurs throughout both: i) the border of the fracture, through a surface area of length L_l and height equal to the actual aperture $h(t)$, and ii) the two walls through a surface area A_l. As a simplification, we assume that the details of the fluid flow in the surrounding matrix can be neglected and that the pressure gradient controlling the leak-off is of order $(p-p_0)/l_0$, l_0 being a characteristic length of the process and p_0 a reference pressure within the matrix. The leak-off fluid velocity is assumed equal to

$$u = \left(\frac{k}{\mu_{eff}}\right)^{1/n} \frac{(p-p_0)^{1/n}}{l_0^{1/n}}, \tag{33}$$

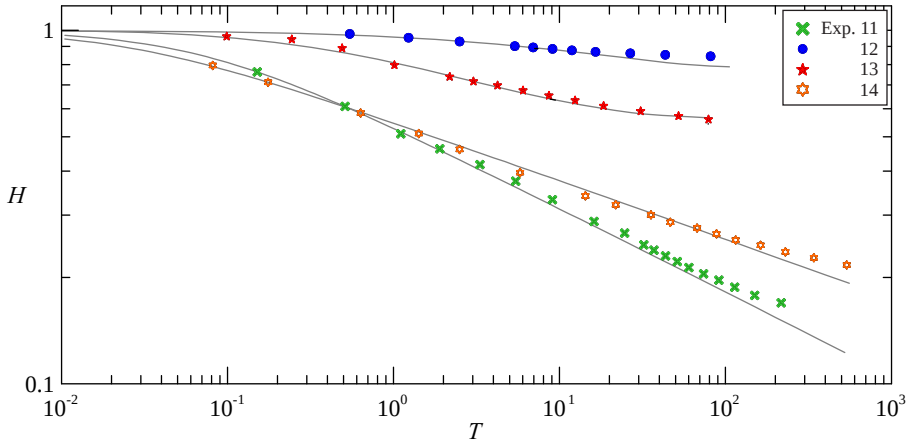

FIG. 14. Experimental results for non-Newtonian shear-thinning fluid, with parameters listed in table I. Symbols represent the experimental data, curves are the theory. Expts. 11 and 14 are with zero exit pressure, Expts. 12-13 are with non-zero exit pressure.

where k is the permeability of the matrix and μ_{eff} is the effective viscosity, with[41]

$$\frac{k}{\mu_{eff}} \equiv \Lambda k^{(1+n)/2},$$
$$\Lambda = \frac{1}{2C_t}\left(\frac{50}{3}\right)^{(n+1)/2}\left(\frac{n}{3n+1}\right)^n \frac{\phi^{(n-1)/2}}{\tilde{\mu}}, \quad (34)$$

where C_t is the tortuosity equal to[42] $C_t = (25/12)^{(n+1)/2}$. Leak-off can occur along the fracture edge of height $h(t)$, or diffusely through the fracture walls as a consequence, e.g., of pre-existing fractures.

When modified by adding sink terms, eq. (11) becomes

$$\frac{\mathrm{d}h(t)}{\mathrm{d}t} = \frac{1}{2^{(1+n)/n}(2n+1)\tilde{\mu}^{1/n}} h(t)^{(2n+1)/n}\left|\frac{\partial p(x,t)}{\partial x}\right|^{1/n-1} \times \frac{\partial^2 p(x,t)}{\partial x^2} - \chi_1 h(t)(p-p_0)^{1/n} - \chi_2 (p-p_0)^{1/n}, \quad (35)$$

where $\chi_1 = [M^{-1/n}L^{1/n}T^{2/n-1}]$ is

$$\chi_1 = \frac{L_l}{L}\left(\frac{k}{l_0\mu_{eff}}\right)^{1/n}, \quad (36)$$

and $\chi_2 = [M^{-1/n}L^{1+1/n}T^{2/n-1}]$ is

$$\chi_2 = \frac{A_l}{L}\left(\frac{k}{l_0\mu_{eff}}\right)^{1/n}. \quad (37)$$

Assuming that the reference pressure within the matrix is the well bore pressure, i.e. $p_0 = p_e$, eq. (35) becomes in dimensionless form

$$\frac{\mathrm{d}H(T)}{\mathrm{d}T} = H(T)^{(2n+1)/n}\left|\frac{\partial P(X,T)}{\partial X}\right|^{(1-n)/n}\frac{\partial^2 P(X,T)}{\partial X^2} - \tilde{\chi}_1 H(T)P(X,T)^{1/n} - \tilde{\chi}_2 P(X,T)^{1/n}, \quad (38)$$

where $\tilde{\chi}_1 = \chi_1 t_c p_c^{1/n}$ and $\tilde{\chi}_2 = \chi_2 h_0^{-1} t_c p_c^{1/n}$ are dimensionless coefficients.

The integral equation (14) and the boundary and initial conditions (15) still hold. We notice that in order to guarantee that $\partial P(1,T)/\partial X = 0$ we assume that no leak-off from the border of the fracture occurs at $X = 1$.

The numerical solution is obtained with a code written in Mathematica, with a parametric solver for $P(X,T)$ as a function of $\tilde{\chi}_1$ of $\tilde{\chi}_2$, n, H_{i+1}, H_i, Δt, where H_i is the value of H at time $i\Delta t$. At each time step, only H_{i+1} is free, all the other parameters are known. Hence, at each step:

- the pressure $P(X)_{i+1}$ is estimated by solving eq.(38) in parametric form and approximating the time derivative with $\dot{H} \approx (H_{i+1} - H_i)/\Delta t$, with $P(0)_{i+1} = 0$ and $P'(1)_{i+1} = 0$; H_{i+1} is the free parameter and $H_0 = 1$. Note that the algorithm guarantees a correct treatment of the boundary conditions on the pressure at the inlet and on the pressure gradient at the outlet, which would otherwise appear as hill-posed and requiring for shooting method after converting the problem to an initial value problem.
- The pressure field is numerically integrated in parametric form in the space domain $[0,1]$; the free parameter is H_{i+1}.
- The parametric integral is used in eq.(14) and the equality is forced with a Newton method to estimate H_{i+1}.
- The procedure is repeated at the next time step.

An example code in Wolfram Mathematica 11 is available in https://github.com/sandrolongo2/sandrocodes. A fully explicit advancement in time with an adapted time step guarantees an adequate reproduction of the analytic solution for $\tilde{\chi} = \tilde{\chi}_2 = 0$, see figure 15 showing the results for different combinations of the two parameters controlling leak-off. The dotted green curve and the thick red curve are the analytical solution and the numerical computation, respectively, for the case without leak-off. The remaining curves, associated with

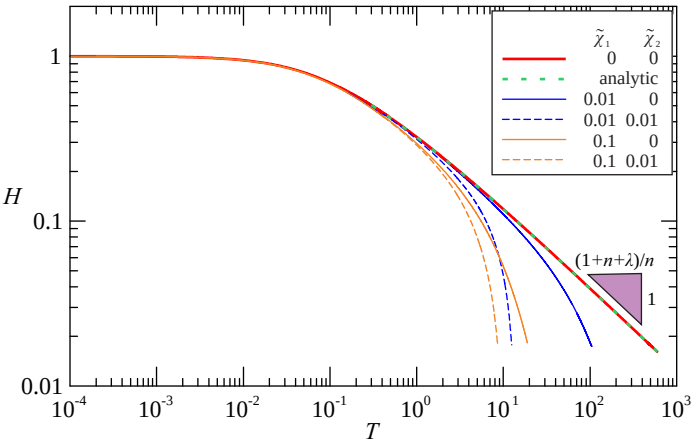

FIG. 15. Dimensionless fracture aperture versus time for $P_e = 0$, $F_0 = 0$, $n = 1$, $\lambda = 1.37$ and different combinations of $\tilde{\chi}_1$ and $\tilde{\chi}_2$. The asymptotic decay for $\tilde{\chi}_1 \neq 0$ and $\tilde{\chi}_2 = 0$ is exponential.

either non-zero $\tilde{\chi}_1$ or non-zero $\tilde{\chi}_2$, show the late-time decay is strongly influenced by the leakage effects, with a faster closure of the fracture with respect to the absence of leakage. The effect of the two different leak-off modes is very similar, although the first mode reduces its effect more rapidly due to both the reduction in pressure in the fracture and the progressive closure of the fracture itself; in the second mode it is assumed that the leakage area is invariant and therefore the decay of the effect is due only to the drop in pressure over time.

V. CONCLUSIONS

Our study tackles the quantitative characterization of the flow back phenomenon of a power-law non-Newtonian fluid taking place in a plane, smooth rock fracture characterized by closing walls associated with various degrees of elasticity. The Newtonian fluid is included as a special case. Closed-from expressions for the fracture aperture, pressure field, discharge rate and drainage time are made available for rigid walls as functions of outlet pressure, overload and recovery rate, and rheological parameters. Our result belong to the category of simplified models and may be used to infer key tendencies and inform upscaling approaches.

Two specific laboratory apparata were built, and an experimental campaign was devised to reproduce the theoretical hypotheses as closely as possible, overcoming the difficulties inherent in the control of the elastic reaction and with an adequate seal, reducing friction to a minimum, carefully checking that there was adequate air venting during the filling phase to avoid trapped air bubbles. The accuracy of the piston and cylinder geometry is a key element of the experimental work, since the dependence of the flow rate on the third power of the fracture opening (for a Newtonian fluid) amplifies the uncertainties by a factor of 3: the uncertainty in the value of h is tripled when calculating the uncertainty in the value of the flow rate. Special care was also taken with the test fluid, both when creating the mixture and when measuring the rheological parameters, by carefully choosing the interpolation range of the power-law model based on the expected range of shear rate. This is a consequence of the fact that the power-law model, like other rheological laws, is an approximation of the real constitutive equation of non-Newtonian fluids and yields different values of the consistency index and of the flow behaviour index when the model is fitted to different ranges of shear rate. Theoretical results were confirmed by our experiments, generally with a good match and minor under- or over-estimation in the order of a few percent.

Further particular conclusions may be drawn from our work:

- The special case of zero outlet pressure and overload has a simple, explicit closed-form solution tending asymptotically to total closure and zero discharge; its late-time behaviour shows a scaling $t^{-n/(n+\lambda+1)}$ for the aperture and $-(2n+\lambda+1)/(n+\lambda+1)$ for the discharge. These exponents clearly elucidate the dependency from flow behaviour index n and exponent λ modulating the wall reaction: very shear-thinning fluids (smaller n) and reactive walls (larger λ) are associated with a more gradual closure.

- The solution for the general case of non-zero outlet pressure p_e and overload f_0 tends asymptotically to a constant value proportional to $(p_e - f_0)^{1/\lambda}$.

- The dimensionless drainage time T_Y required to recover $Y\%$ of the fluid initially residing in the system decreases with increasing n and P_e and decreases with λ, and the differences are greater the more the fluid is shear-thinning. For recovery values close to 100%, T_Y is extremely sensitive to variations of model parameters.

- Experiments can also be conducted on a small geometric scale, but with adequate control of all test steps to limit disturbances and reduce the uncertainty of the results.

- The use of two different apparata allowed exploring both sub- and supra-linear wall reactions and showed the lack of scale effects.

The body of experimental and theoretical work on Newtonian and non-Newtonian power-law backflow from a fracture with relaxing walls towards a central well or borehole in the two limit flow configurations (plane and radial) allows to describe the phenomenon in a quite comprehensive way within the framework of the single fracture conceptualization. Problem variables are described as functions of system parameters in dimensionless form without the need of specifying any dimensionless number for a Newtonian fluid[11], and quantifying the only flow behaviour index n for power-law fluids, having a two-parameter constitutive equation (Chiapponi *et al.*[32] and this paper); when a three-parameter rheology such as the Ellis model is adopted the need for an additional dimensionless quantity, namely the ratio between the characteristic shear stress of the Ellis fluid τ_0 and the rock modulus of elasticity E,

arises[33]. Similarly, the incorporation of slip effects, relatively common in non-Newtonian flows, would give rise to one or more dimensionless numbers. Another intriguing option is to optimize system performance in terms of geometry and/or rheology using specific metrics , or model inertial flow[43]. Finally, the need for incorporating uncertainty into modelling of fracking phenomena has recently been brought to attention in the literature[44].

ACKNOWLEDGMENTS

Vittorio Di Federico gratefully acknowledges the financial support from Università di Bologna Almaidea 2017 Linea Senior grant. Sandro Longo gratefully acknowledges the financial support from Anton Paar for co-funding the Anton Paar DMA 5000 density meter and TwinDrive MCR 702 rheometer. The Department of Engineering and Architecture of the University of Parma, with its Rheometrica lab, is in the list of the Anton Paar reference research centres for the testing and development of experimental apparatus in the field of rheology. The cost of the equipment used for this experimental investigation was partly supported by the University of Parma through the Scientific Instrumentation Upgrade Programme 2018. The authors declare that they have no known competing financial interests or personal relationships that could have appeared to influence the work reported in this paper. There are no data sharing issues since all the numerical information is provided in the figures produced by solving the equations in the paper.

Appendix A: Late-time approximations for $P_e - F_0 = 0$

For late time ($T \gg 1$), equations (21) and (22) simplify to

$$H(T) \approx (n+2)^{-1/(1+n+\lambda)}(1+n+\lambda)^{-n/(1+n+\lambda)}T^{-n/(1+n+\lambda)}, \tag{A1}$$

$$P(X,T) \approx \frac{(n+2)^{(n+1)/(1+n+\lambda)}(1+n+\lambda)^{-\lambda n/(1+n+\lambda)}}{n+1} \times T^{-\lambda n/(1+n+\lambda)} \times \left[1-(1-X)^{n+1}\right]. \tag{A2}$$

Appendix B: Early- and late-time approximations for $P_e - F_0 > 0$

For early time ($T \ll 1$) eq. (23) reduces to

$$T \approx \frac{1}{(n+2)^{\frac{1}{n}}(1+n+\lambda)} \times \left[\frac{1}{H^{\frac{1+n+\lambda}{n}}}\left(1+\frac{1+n+\lambda}{n(1+n)(1+\lambda)}\frac{P_e-F_0}{H^{\lambda}}\right)\right]\Bigg|_1^H. \tag{B1}$$

For late time ($T \gg 1$) the approximation of eq. (23) is

$$T \approx \frac{H^{-(1+n+\lambda)/n}}{(n+2)^{1/n}\lambda(1-n)}\left(1-\frac{P_e-F_0}{H^{\lambda}}\right)^{1-1/n} + \frac{H^{-(1+n+\lambda)/n}}{(n+2)^{1/n}(1+n+\lambda)}\frac{\Gamma(1-1/n)\Gamma((\lambda+1)(n+1)/(n\lambda))}{\Gamma(1+(1+n)/(n\lambda))}, \tag{B2}$$

which is singular for $n = 1$. The symbol $\Gamma(\cdot)$ is the Gamma function.

Appendix C: Identity for specific value of the hypergeometric function ${}_2F_1$

The following identity holds for any positive z[45]

$${}_2F_1(1,3;4;z) = -\frac{3}{2z^3}\left[z(z+2)+2\ln(1-z)\right]. \tag{C1}$$

DATA AVAILABILITY

The data that support the findings of this study are available from the corresponding author upon reasonable request.

REFERENCES

[1] R. Sahai and R. G. Moghanloo, "Proppant transport in complex fracture networks - a review," Journal of Petroleum Science and Engineering **182**, 106199 (2019).

[2] M. Economides, D. Mikhailov, and V. Nikolaevskiy, "On the problem of fluid leakoff during hydraulic fracturing," Transport in Porous Media **67**, 487–499 (2007).

[3] D. Birdsell, H. Rajaram, and D. D. H. Viswanathan, "Hydraulic fracturing fluid migration in the subsurface: a review and expanded modeling results," Water Resources Research **37**, 1–30 (2015).

[4] H. Hofmann, S. Weides, T. Babadagli, G. Zimmermann, I. Moeck, J. Majorowicz, and M. Unsworth, "Potential for enhanced geothermal systems in alberta, canada," Energy **69**, 578–591 (2014).

[5] D. S. Bolintineanu, R. R. Rao, J. B. Lechman, J. A. Romero, C. F. Jove-Colon, E. C. Quintana, S. J. Bauer, and M. D. Ingraham, "Simulations of the effects of proppant placement on the conductivity and mechanical stability of hydraulic fractures," International Journal of Rock Mechanics and Mining Sciences **100**, 188–198 (2017).

[6] L. Britt, "Fracture stimulation fundamentals," Journal of Natural Gas Science and Engineering **8**, 34–51 (2012).

[7] E. Detournay, "Mechanics of hydraulic fractures," Annu. Rev. Fluid Mech. **48**, 311–339 (2016).

[8] C. Clarkson, B. Haghshenas, A. Ghanizadeh, F. Qanbari, J. Williams-Kovacs, N. Riazi, C. Debuhr, and H. Deglint, "Nanopores to megafractures: Current challenges and methods for shale gas reservoir and hydraulic fracture characterization," Journal of Natural Gas Science and Engineering , 513–535 (2016).

[9] O. E. Agwu, J. U. Akpabio, S. B. Alabi, and A. Dosunmu, "Artificial intelligence techniques and their applications in drilling fluid engineering: A review," Journal of Petroleum Science and Engineering **167**, 300–315 (2018).

[10]C.-Y. Lai, Z. Zheng, E. Dressaire, G. Ramon, H. Huppert, and H. Stone, "Elastic relaxation of fluid-driven cracks and the resulting backflow," Physical Review Letters **15**, 24–36 (2016).
[11]A. Dana, Z. Zheng, G. G. Peng, H. A. Stone, H. E. Huppert, and G. Z. Ramon, "Dynamics of viscous backflow from a model fracture network," Journal of Fluid Mechanics **836**, 828–849 (2018).
[12]M. Kobchenko, A. Hafver, E. Jettestuen, O. Galland, F. Renard, P. Meakin, B. Jamtveit, and D. K. Dysthe, "Drainage fracture networks in elastic solids with internal fluid generation," EPL (Europhysics Letters) **102**, 66002 (2013).
[13]C. Abugattas, A. Aguirre, E. Castillo, and M. Cruchaga, "Numerical study of bifurcation blood flows using three different non-Newtonian constitutive models," Applied Mathematical Modelling **88**, 529–549 (2020).
[14]A. Dana, G. G. Peng, H. A. Stone, H. E. Huppert, and G. Z. Ramon, "Backflow from a model fracture network: an asymptotic investigation," *Journal of Fluid Mechanics*, Journal of Fluid Mechanics **864**, 899–924 (2019).
[15]Z. Zhu, J. Liu, H. Liu, M. Wu, and Z. Song, "Numerical investigation of single- and two-phase flow in porous media with a bifurcated fracture," Physics of Fluids **33**, 052117 (2021).
[16]A. Barbati, J. Desroches, A. Robisson, and G. McKinley, "Complex fluids and hydraulic fracturing," Annu. Rev. Chem. Biomol. Eng. **7**, 415–453 (2016).
[17]A. Osiptov, "Fluid mechanics of hydraulic fracturing: a review," Journal of Petroleum Science and Engineering **156**, 513–535 (2017).
[18]Y. Lester, T. Yacob, I. Morrissey, and K. G. Linden, "Can we treat hydraulic fracturing flowback with a conventional biological process? the case of guar gum," *Environmental Science & Technology Letters*, Environ. Sci. Technol. Lett. **1**, 133–136 (2014).
[19]A. M. Linkov, "On comparison of thinning fluids used for hydraulic fracturing," International Journal of Engineering Science **10**, 14–23 (2014).
[20]C. Yao, Q. H. Jiang, and J. F. Shao, "A numerical analysis of permeability evolution in rocks with multiple fractures," Transport in Porous Media **108**, 289–311 (2015).
[21]M. M. Rahman and S. S. Rahman, "Studies of hydraulic fracture-propagation behavior in presence of natural fractures: Fully coupled fractured-reservoir modeling in poroelastic environments," International Journal of Geomechanics **13**, 809–826 (2013).
[22]R. Bird, W. Stewart, and E. Lightfoot, *Transport Phenomena. 2nd Edition* (John Wiley & Sons Ltd., New York, 2002).
[23]J. I. Adachi and E. Detournay, "Plane strain propagation of a hydraulic fracture in a permeable rock," Engineering Fracture Mechanics **75**, 4666 – 4694 (2008).
[24]D. I. Garagash, "Transient solution for a plane-strain fracture driven by a shear-thinning, power-law fluid," *International Journal for Numerical and Analytical Methods in Geomechanics*, Int. J. Numer. Anal. Meth. Geomech. **30**, 1439–1475 (2006).
[25]D. Mikhailov, M. Economides, and V. Nikolaevskiy, "Fluid leakoff determines hydraulic fracture dimensions: Approximate solution for non-Newtonian fracturing fluid," International Journal of Engineering Science **49**, 809–822 (2011).
[26]E. Dontsov, "Scaling laws for hydraulic fractures driven by a power-law fluid in homogeneous anisotropic rocks," Int J Numer Anal Methods Geomech. **43**, 519–529 (2019).
[27]A. Lakhtychkin, D. Eskin, and O. Vinogradov, "Modelling of transport of two proppant-laden immiscible power-law fluids through an expanding fracture," The Canadian Journal of Chemical Engineering **90**, 528–543 (2012).
[28]M. Perkowska, M. Wrobel, and G. Mishuris, "Universal hydrofracturing algorithm for shear-thinning fluids: Particle velocity based simulation," Computers and Geotechnics **71**, 310–337 (2016).
[29]M. Wrobel, "On the application of simplified rheological models of fluid in the hydraulic fracture problems," International Journal of Engineering Science **150**, 103275 (2020).
[30]M. Wrobel, G. Mishuris, and P. Papanastasiou, "On the influence of fluid rheology on hydraulic fracture," International Journal of Engineering Science **158** (2021).
[31]L. Pereira and B. Lecampion, "A plane-strain hydraulic fracture driven by a shear-thinning Carreau fluid," International Journal for Numerical and Analytical Methods in Geomechanics (2021).
[32]L. Chiapponi, V. Ciriello, S. Longo, and V. Di Federico, "Non-Newtonian backflow in an elastic fracture," Water Resources Research **55**, 10144–10158 (2019).
[33]V. Ciriello, A. Lenci, S. Longo, and V. Di Federico, "Relaxation-induced flow in a smooth fracture for Ellis rheology," Advances in Water Resources **152**, 103914 (2021).
[34]R. Medina, R. Detwiler, R. Prioul, W. Xu, and J. Elkhoury, "Settling and mobilization of sand-fiber proppants in a deformable fracture," Water Resources Research **54**, 9964–9977 (2019).
[35]N. Ali, A. Abbasi, and I. Ahmad, "Channel flow of Ellis fluid due to peristalsis," AIP Advances **5**, 097214 (2021).
[36]S. Longo, V. Di Federico, and L. Chiapponi, "A dipole solution for power-law gravity currents in porous formations," Journal of Fluid Mechanics **778**, 534–551 (2015).
[37]A. D. Kerr, "Elastic and Viscoelastic Foundation Models," Journal of Applied Mechanics **31**, 491–498 (1964).
[38]I. S. Gradshteyn and I. M. Ryzhik, *Table of integrals, series, and products* (Academic Press, 2014).
[39]S. Holditch, "Hydraulic fracturing: Overview, trends, issues," Drilling contractor **July-August 2007**, 116–118 (2007).
[40]S. Longo and V. Di Federico, "Unsteady flow of shear-thinning fluids in porous media with pressure-dependent properties," Transport in Porous Media **110**, 429–447 (2015).
[41]V. Ciriello, S. Longo, L. Chiapponi, and V. Di Federico, "Porous gravity currents: a survey to determine the joint influence of fluid rheology and variations of medium properties," Advances in Water Resources **92**, 105–115 (2016).
[42]H. Pascal, "Nonsteady flow of non-Newtonian fluids through a porous medium," International Journal of Engineering Science **21**, 199–210 (1983).
[43]F. J. Valdés-Parada and D. Lasseux, "Flow near porous media boundaries including inertia and slip: A one-domain approach," Physics of Fluids **33**, 073612 (2021).
[44]A. A. Quosay, D. Knez, and J. Ziaja, "Hydraulic fracturing: New uncertainty based modeling approach for process design using monte carlo simulation technique," PLOS ONE **15**, 1–18 (2020).
[45]Wolfram, http://functions.wolfram.com/HypergeometricFunctions/Hypergeometric2F1/03/ (2020), accessed on 21/02/2020.